High-Lift Design for a Forward Swept Natural Laminar Flow Wing

D. Keller

Institut für Aerodynamik und Strömungstechnik,
Deutsches Zentrum für Luft- und Raumfahrt,
Lilienthalplatz 7, 38108 Braunschweig

Abstract

The scope of the paper is to present the results of a RANS based aerodynamic high-lift design for a natural laminar flow wing with negative sweep. The chosen high-lift system consists of a Krueger leading edge flap with shielding function and a fixed-vane trailing edge flap. The design was first optimized in two main wing sections and then verified by 3D RANS siumlations of a wing-body model. Finally, engines were added to the geometric model in order to estimate the high-lift performance of the landing configuration. With a maximum lift coefficient of $C_L = 2.85$ for the wing-body model with engine, the target from the preliminary aircraft design was reached. Further potential for improvement was found in the optimization strategy and the shape of the fuselage-wing junction.

1 Introduction

The idea of maintaining the boundary layer on parts of the aircraft laminar is a promising approach in order to further reduce the aircraft's drag. In this context, the main wing is particularly interesting due to its wetted surface size at comparatively small Reynolds numbers. Therefore, the DLR is investigating an aircraft configuration with natural laminar flow wings. Due to its forward-swept wings, cross-flow instabilities and attachment line transition can be delayed to higher cruise speeds and the aircraft's cruise efficiency is increased. However, this type of wing makes a high-lift design novel and challenging due to various reasons.

Obviously, the main purpose of the high-lift devices remains the improvement of the climb rate at take-off and the reduction of the stall speed during landing. However, since insects are a potential source of wing surface contamination near ground, which may lead to premature laminar-turbulent transition

during cruise flight, the leading edge device shall also function as shielding device for the clean wing. Besides this additional requirement, the design conditions are also more constrained. The leading edge device must not introduce discontinuities such as steps in regions, where laminar flow is desired. Furthermore, the small leading edge radius typical for laminar flow airfoils potentially impacts the maximum lift capabilities in a negative way. Besides, it also constraints the design of the leading edge device as it reduces the available space. The negative sweep is another important aspect, which affects the high-lift design. It leads to a shift of the wing load towards the root and thus increases the adverse pressure gradient in a region, which is already prone to corner flow separation. Additionally, the flow above the main wing tends to move towards the wing tip, creating the effect of a diverging channel at the fuselage-wing junction, which further exacerbates the flow conditions at the wing root. Besides, the negative sweep leads to a highly swept trailing edge, which may also reduce lift generation.

Little documentation [1] is found on the high-lift design for forward swept wings. However, some studies exist on high-lift aerodynamics for laminar flow wings in general. Bright et al. examined leading edge concepts for a laminar cruise airfoil [2]. They achieved a maximum section lift coefficient ($C_{l,max}$) of 5.2 for a configuration with plain trailing edge flap, morphing droop nose and additional blowing on both high-lift devices. In Europe, several partners investigated passive leading edge devices, such as the droop nose, large slat and slotted Krueger flap in order to find the one, which is suited best for natural laminar flow wings [3, 4, 5, 6, 7]. They found the slotted Krueger flap to perform best in terms of $C_{L,max}$, drag, impact on laminarity and leading edge insect shielding properties. 3D RANS simulations of the resulting optimized high-lift design resulted in a maximum lift coefficient of 2.63, which was sufficiently above

the specified target [6]. In 2016, Franke et al. successfully presented a Krueger flap design for a hybrid laminar flow wing under realistic design constraints [8] and reached maximum section lift coefficients of 3.3 for a hybrid laminar airfoil with Krueger flap and no trailing edge flap.

The underlying paper demonstrates a conventional successive high-lift design approach for the DLR Tu-Lam aircraft configuration based on RANS computations and considering the mentioned challenges. Therefore, a Krueger leading edge flap as well as a dropped hinge fixed-vane trailing edge flap are deployed. The design process begins with an aerodynamic 2D high-lift optimization, considering kinematics and available space. In a second step, the 3D high-lift concept is realized based on the sectional results. Simulations of the wing-body configuration are carried out to verify the expected aerodynamic performance. In the last step, engines are added in order to investigate integration related aspects and make a final evaluation of the high-lift design.

2   Numerical methods

Flow solver   Two different flow solvers were used, which both solve the compressible Reynolds-averaged Navier-Stokes equations based on the finite-volume approach. The block structured FLOWer code [9] was used for the 2D optimizations, whereas the hybrid TAU code [10] was used for the 3D simulations. In both cases, the spatial discretization of the convective fluxes is done with a 2nd-order central scheme. The turbulence effects are modeled with the original Spalart-Allmaras formulation [11]. For the 3D computations, vortical and rotational flow correction based on the Spalart-Shur correction [12] was used.

Optimization algorithm   The optimization of the 2D sections is carried out with a SUBLEX algorithm developed by Rowan [13]. It is based on the Simplex method and thus is a deterministic, gradient free algorithm. The idea of the SUBLEX is to decompose the design space into "low-dimensional subspaces" that the Simplex can be efficiently applied to. The SUB-LEX approach is particularly favorable for multi element high-lift optimizations, as it is robust against noisy objective functions and efficiently handles large numbers of design variables, as it was demonstrated by Wild [14].

3   Geometric model

Figure 1 shows the TuLam aircraft configuration, which was designed with the preliminary design tool PrADO [15]. It has a maximum take-off weight of 70 tons and a design mission range of approximately 2600 nautical miles at a cruise Mach number of $M_{cr} = 0.78$. Table 1 depicts some of the aerodynamic aircraft parameters.
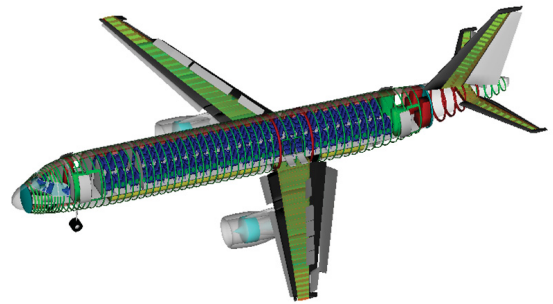

Figure 1: TuLam aircraft configuration (source: A. Hübner, DLR)

Reference area	$122\mathrm{m}^2$
Span	17m
Aspect ratio	9.48
Taper ratio	0.34
Sweep angle (leading edge)	$-17°$

Table 1: Basic geometric parameters of the TuLam configuration

4   High-lift concept

Typically, the aerodynamic high-lift design is driven by the climb performance in take-off configuration and the approach speed in landing configuration while keeping system complexity and weight to a minimum. In case of a natural laminar flow wing, the leading edge device shall also function as a shielding device against contamination by dirt or insects for the clean wing. Furthermore, the leading edge device must not introduce discontinuities such as steps in regions, where laminar flow is desired. A promising approach to fulfill these requirements is to use a Krueger flap [3]. Since it is deployed from the lower side of the wing, the upper surface remains smooth. Furthermore the Krueger flap can be used as shielding device for the fixed leading edge. The type of Krueger flap ranges from a simple one, which was already used on the Boeing 707 to a rather complex variable camber (VC) Krueger flap, known from the Boeing 747. For

the present study, a slotted bull-nose Krueger was chosen, which is thought to be a good trade-off between maximum lift performance and system complexity. The slotted bull-nose Krueger was already investigated within the DeSiReH project[6, 7] and the AFLoNEXT project[8], where its high-lift performance was comparable to the one of a slat.

The large trailing edge sweep of the main wing leads to the assumption that a single slotted flap might not deliver a sufficiently high maximum lift coefficient. A double slotted flap promises higher maximum lift coefficients at the cost of increased system complexity and weight. A compromise between a high maximum lift coefficient and low system weight is the fixed-vane flap on a dropped hinge kinematics. The fixed-vane flap is a double slotted flap, at which the smaller fore element, the vane, is fixed to the main flap. Due to the avoidance of additional kinematics between the vane and the flap and the use of a rather simple dropped hinge kinematics, the system complexity is reduced, albeit parts of the aerodynamic performance gains of a multi element trailing edge flap are kept. The drawback of this type of trailing edge device is its lack of variability. Due to the dropped-hinge kinematics, it is deployed on a circular path and the combination of area increase, flap deflection, gap and overlap cannot be optimized independently for more than one flap position. The fixed-vane flap was already used on various commercial aircraft such as the Boeing 707, DC-8, DC-9 and the MD-80 [3].

At the end of the flap, an additional plain flap with a chord length of $c_{PF}/c = 0.1$ is integrated in order to control the pressure distribution in cruise configuration. The plain flap can be also used to increase the variability in high-lift configuration.

5 Design philosophy

The high-lift design process begins with a rough outline of the main wing's high-lift system. The TuLam model is supposed to have an inboard and outboard Krueger flap, which are separated by the engine pylon (figure 2). The fixed-vane flap extends from the belly fairing to the inner end of the aileron at $\eta = 0.82$. Even though a single flap along the entire span might not be feasible from a structural point of view, the trailing edge device shall not contain any spanwise gaps and can therefore be seen as one from an aerodynamic perspective. The resulting outline of the high-lift design delivers the maximum outboard position of the Krueger flap, which is used to estimate design constraints due to clearance and segregation rules. Af-

ter delineating the spanwise dimensions of the high-lift system, characteristic sections are extracted from the clean wing. Two sections at $\eta = 0.22$ and $\eta = 0.56$ are chosen, here, representing the main wing's inboard and outboard region, respectively. The high-lift design is then parameterized on these sections, whereas design constraints due to clearance and segregation rules are considered for the design space, and subsequently optimized. Since the trailing edge flap is continuous along the span, it cannot be independently optimized for both sections. Therefore, the optimization of the entire high-lift system is conducted for one section, first. Afterwards, the parameters of the Krueger flap are optimized for the second section, whereas the parameters of the trailing edge device are taken from the optimization results of the first section. Since many design parameters are non-dimensionalized with the chord length and the airfoil of the outboard section is thinner than the inboard one, the outboard section is more restrictive regarding the feasibility of the parameters. Furthermore, the extent of the high-lift system on the outboard wing is larger than the one on the inboard wing. Consequently, the outboard section was optimized first. Based on the results of the sectional optimization, the high-lift design is applied to the full wing and the 2D optimization results can be verified by simulations of the wing-body configuration. Furthermore, wing-body integration aspects can be assessed. In the final step, the engine is integrated into the model and the final estimation of the aircraft's high-lift performance is carried out.

The chosen design philosophy was already successfully demonstrated in previous studies, e.g. see [16].
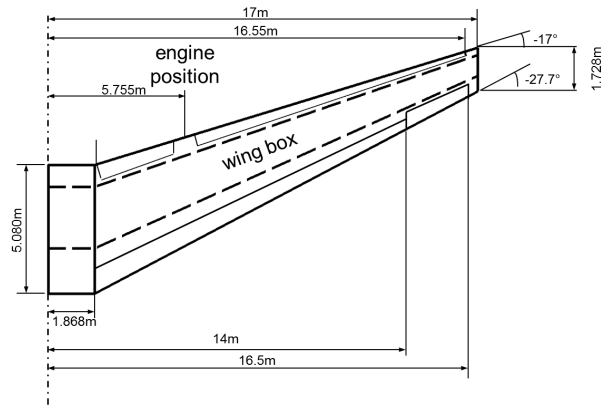

Figure 2: Spanwise extends of the high-lift design

5.1 Sectional high-lift optimization

For the sectional optimization of the high-lift design, the infinite swept wing analogy is used. The design

sections, which are in in-flight direction are extracted from the 3D planform and transformed to a plane normal to the leading edge. As a result, the relative thickness of the airfoil is increased (eq. 1). Furthermore, the freestream conditions are adapted using the sweep angle of the leading edge ϕ_{LE} (eq. 2, 3):

$$Y_{2D} = \frac{Z_{3D}}{\cos\phi_{LE}} \tag{1}$$

$$M_{2D} = M_{3D} * \cos\phi_{LE} \tag{2}$$

$$Re_{2D} = Re_{3D} * \cos^2\phi_{LE} \tag{3}$$

The high-lift design is then optimized for these sections normal to the leading edge.
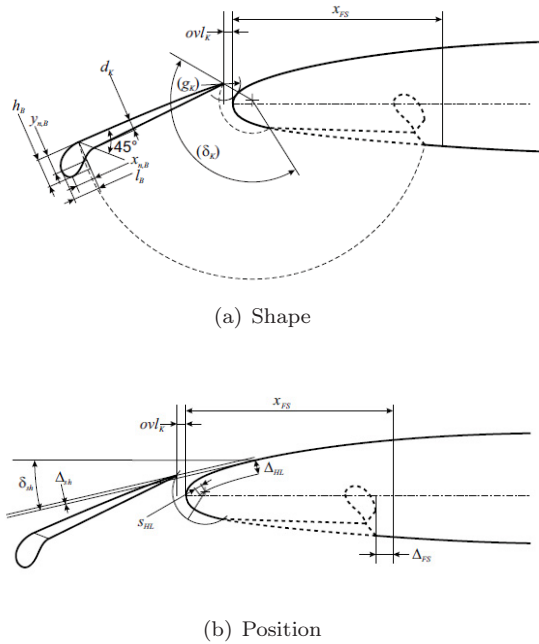
(a) Shape

(b) Position

Figure 3: Parametrization of the Krueger flap [17]

The Krueger flap is parameterized by 10 design parameters, considering its kinematics. While 5 parameters describe the shape of the Krueger flap, the other 5 define its position and deflection, as it is depicted in figure 3(a) and 3(b), respectively. The parameters are constraint due to space limitations in front of the front spar, which is located at $c_{FS}/c = 0.17$. In order to guarantee the feasibility of integration, assumptions regarding necessary space for the kinematics and device clearance were made based on results from a previous design study [8]. An additional constraint arises from the shielding requirement. Based on the work of Tamigniaux [18], who found only little contamination for particles impacting at angles

less than 7°, the Krueger flap shall be positioned in a way that it guarantees the shielding of the clean wing nose up to the position, where the tangent of the upper surface is at 13 degree angle to the main wing chord.

The fixed-vane flap is parameterized by 19 design variables as seen in figure 4. Design parameters for the vane length and parameters for the slot between the vane and the aft flap, such as gap and overlap define the basic setup. The hinge point position and the setting for the landing configuration are defined by the gap and overlap between the main wing and the vane and the maximum deflection angle. Additional parameters describe the shape of the flap elements. In order to avoid collisions between the flap elements and the main wing, the upper surface of the flap elements have to stay below the circular arc, which is defined by the hinge point and the main wing's trailing edge. In take-off position, the gap between the main wing and the vane shall be sealed for drag minimization. Therefore, a part of the vane's upper surface is defined by this circular arc.

Besides the 19 parameters, describing the fixed-vane flap, the rear part of the flap can be deflected by one extra parameter. The optimization aimed at maximizing the maximum lift coefficient: $f_{obj} = -C_{l,max}$ at the local Mach and Reynolds numbers of $M_{3D,I/B} = 0.2$, $Re_{3D,I/B} = 19.6 * 10^6$ and $M_{3D,O/B} = 0.2$ and $Re_{3D,O/B} = 15.8 * 10^6$, for the inboard and outboard sections, respectively.
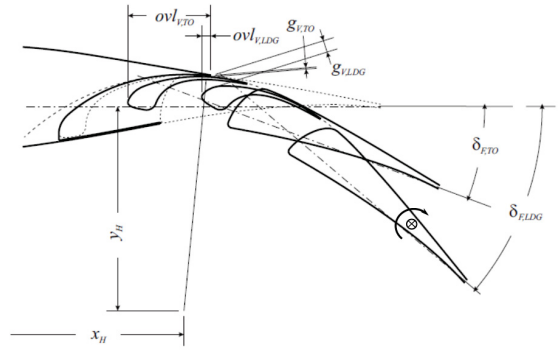

Figure 4: Parametrization of the fixed-vane flap [17]

6 Results

6.1 Optimization results

6.1.1 Outboard section

The high-lift optimization of the outboard section considers parameters of the Krueger flap and the

fixed-vane flap. In the baseline case, the plain flap at the flap's rear is undeflected, leading to 29 design parameters. In a second approach, the deflection of the plain flap is an additional design parameter. Both optimizations needed around 600 function calls to converge, whereas both cases ran into the design space limitations regarding the Krueger flap.

On the outboard wing, the Krueger geometry is significantly constrained by the limited available space. Since the segregation and clearance rules are formulated in absolute values and have to be valid for the entire span, the non-dimensionalized constraints become large. The limitations in chordwise direction are most critical as they limit the size of the Krueger panel. The rearmost point of the retracted panel is constrained by the position of the frontspar and the minimum clearance Δ_{FS}. Both optimizations ran into the minimum clearance constraint, which eventually limited the further reduction of the objective function. Towards the front the panel's extend is prescribed by the hinge point position and the Krueger's trailing edge position in case of deflection. Since the Krueger flap is used as shielding device, the deflection angle cannot be independently defined and is a function of the gap/overlap and the position of the hinge point. Moving the hinge point position in downstream direction reduces the Krueger panel size and increases the deflection angle. Consequently, the extension of the Krueger panel towards the front is a trade-off between panel size, gap/overlap and deflection angle. Therefore, the resulting deflection angle of the Krueger panel is rather high and the angle of incidence between the Krueger flap's chord and the clean airfoil's chord is small (figure 5). However, due to the large bull nose, the angle of incidence still reaches $\Theta_{KR,BSL} = 43.5°$. The large bull nose with its rather low curvature is another important trend. Its effect of improving the deflection angle as well as the low nose curvature reduce the suction peak and therefore lead to higher maximum angles of attack. However, the size of the bull nose is limited by the minimum clearance condition between the Krueger flap and the upper surface panel in retracted position. Comparing the baseline configuration and the one with the additional plain flap deflection shows only little differences in the Krueger geometry. The most significant one is a slight increase in gap and negative overlap in case of the additional plain flap deflection. The differences in the geometry are more significant at the trailing edge device. The deflection angle of the case with plain flap is slightly lower with $\delta_{F,LDG} = 36.9°$ compared to $\delta_{F,LDG} = 38.2°$ for the baseline case. However, the total camber seems to be almost identical for both cases, as the flap trailing edge positions

are nearly identical. Yet, in case of the plain flap, the camber is more distributed due to the additional plain flap deflection of $\delta_{PF,LDG} = 5.5°$. Furthermore, the relative vane length compared to the length of the entire flap device is slightly reduced in case of the additional plain flap from $c_{Vane}/c_{Flap} = 0.257$ to $c_{Vane}/c_{Flap} = 0.242$.
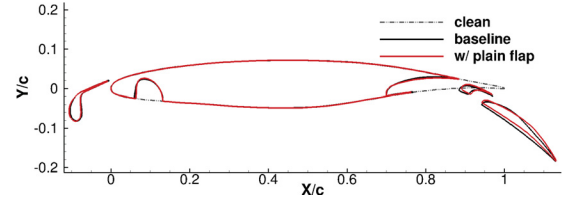

Figure 5: Optimized high-lift geometry of the outboard section

(a) $\alpha = 6°$

(b) $\alpha = 16.5°$
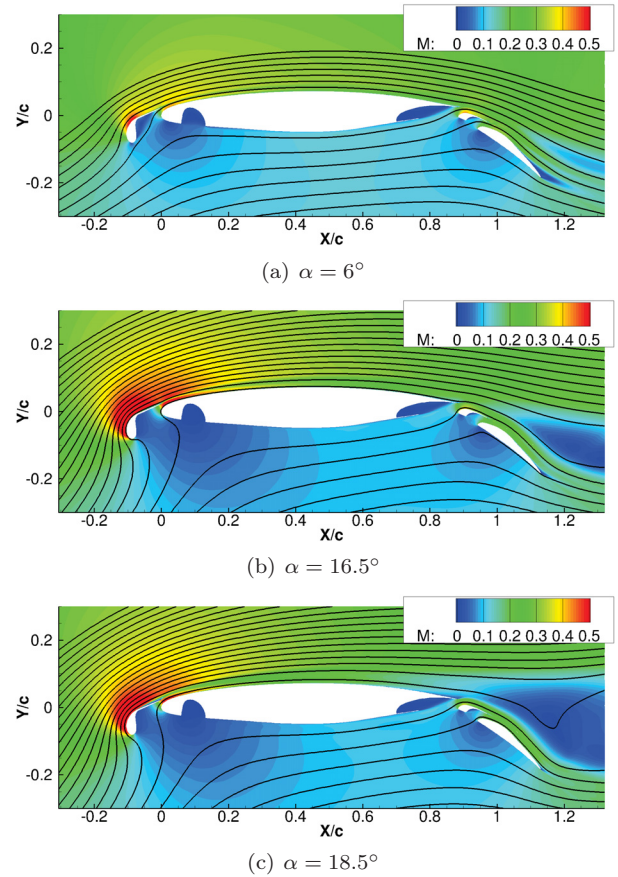
(c) $\alpha = 18.5°$

Figure 6: Flowfield evolution with rising angle of attack for outboard section of the baseline case

Figure 6 shows the flowfield evolution with rising angle of attack for the baseline case. At low angles of attack (figure 6(a)), the flow is partly separated from

the main flap. With rising angle of attack, the circulation of the main element increases, which is indicated by higher Mach number values on the upper side and lower values on the lower side (figure 6(b)). Due to the higher circulation of the main element, the flap is deloaded, as it is described by the slat effect according to Smith [19]. The resulting lower suction peak and the accompanied reduced adverse pressure gradient on the main flap lead to a reattachment of the flow. However, the lift is limited due to the reduced circulation of the flap elements. If the angle of attack is further increased, trailing edge separation occurs at the Krueger flap, which eventually leads to a lift break down (figure 6(c)). The flow topology and the stall mechanism are identical for the case with plain flap.

Figure 7 compares the lift curves of the baseline case and the one with plain flap. The optimization with the plain flap delivers a slightly increased maximum lift coefficient, which is 6 lift counts higher than the one of the baseline case. However, the increased maximum lift coefficient is due to an increased maximum angle of attack. In the linear range, the lift coefficient is actually lower than the one of the baseline case. With $c_L = 4.27$, the maximum lift coefficient is raised by $\Delta c_L = 2.62$ compared to the maximum lift coefficient of the clean airfoil.
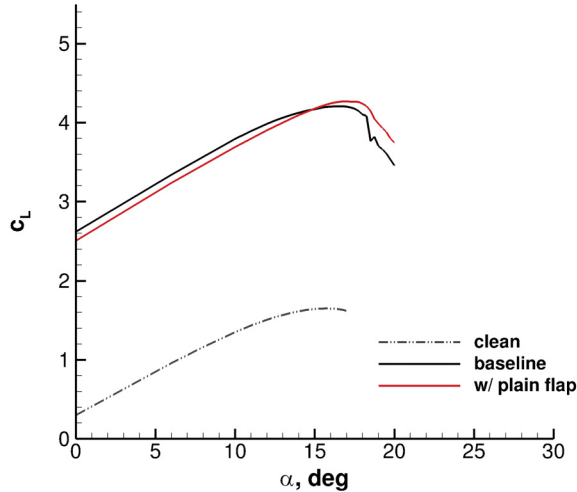

Figure 7: Lift curves of optimized cases

6.1.2 Inboard section

Since the fixed-vane is fixed in the optimizations of the inboard section, both cases only needed roughly 300 runs to converge. The space limitation is less severe in the inboard section, leading to an unconstrained position of the hinge point. As a result,

the angle of incidence of the Krueger flap is larger with $\Theta_{KR,BSL} = 53.6°$ compared to the one at the outboard section (figure 8). Furthermore, the size of the Krueger panel is increased. However, the Krueger panel's size is still limited by the position of the frontspar and the minimum frontspar clearance. Comparing the case with plain flap with the baseline case shows only little differences. The most significant one is a slight increase in the bull nose size. The position of the Krueger flap's trailing edge and the angle of incidence are almost identical with $\Theta_{KR,PF} = 54.0°$.
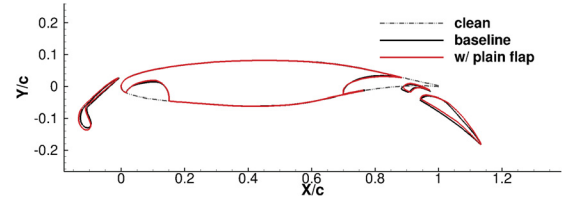

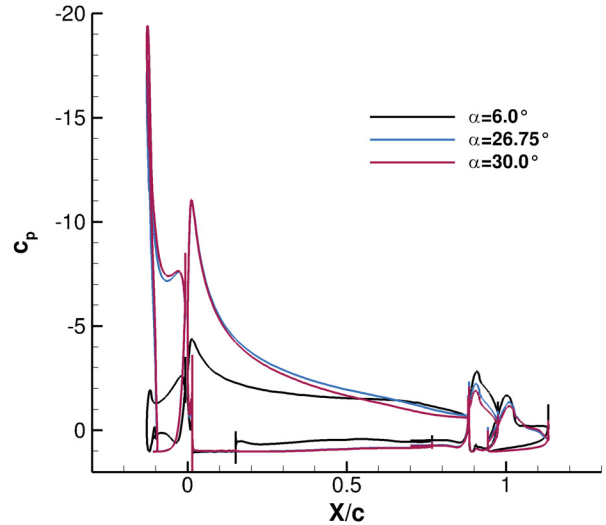Figure 8: Optimized high-lift geometry of the inboard section

Figure 9: Pressure distribution of the optimized inboard section (baseline)

At low angles of attack, the flow topology at the inboard section is similar to the one at the outboard section. The flow is partially separated from the flap, as it is indicated by the pressure plateau near the trailing edge at $\alpha = 6°$ (black line in figure 9). With rising angle of attack, the flow begins to reattach to the flap and the plateau vanishes (blue line). Despite the flow reattachment, the suction peaks of the vane

and the flap decrease due to the increased circulation of the main wing. The pressure distributions at the main element and the Krueger flap are not negatively affected, showing strong suction peaks and a similar pressure coefficient at the main element's trailing edge compared to the one at $\alpha = 6°$. If the angle of attack is further raised to $\alpha = 30°$, the suction peak of the Krueger flap continues to increase (red line). The suction peaks of the trailing edge devices further decrease, whereas the flow remains attached to the vane and the flap. Due to the reduced circulation of the vane and the resulting higher pressure at the vane's nose, the pressure coefficient at the main element's trailing edge is increased and trailing edge separation sets in. Consequently, the suction peak of the main element stops rising. Again, the evolution of the flow topology, including the stall mechanism is identical in case of the additional plain flap.
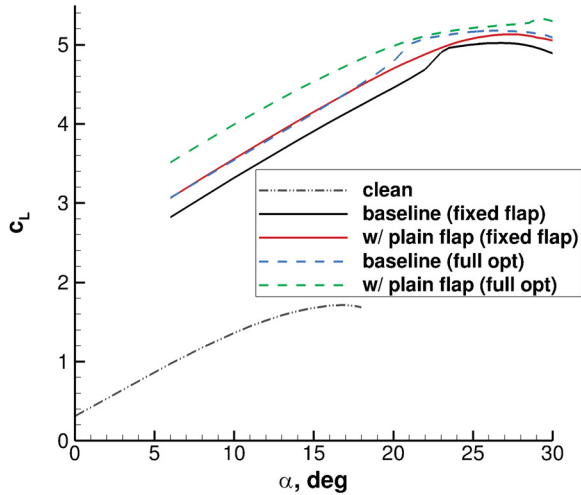

Figure 10: Lift curves of optimized cases in inboard section

Compared to the outboard section, the airfoil of the inboard section is notably thicker and experiences a higher Reynolds number, which might have a positive effect on the maximum lift coefficient. More important however are the better geometries and deflection angles of the Krueger flap, which result from the less constrained optimizations. Consequently, the maximum angle of attack is significantly increased compared to the outboard section, as can be seen in figure 10. Maximum lift is reached at $\alpha_{max} = 26.75°$ for the baseline case (black solid line). With $c_{L,max} = 5.02$, the maximum lift coefficient is raised by $\Delta c_{L,max} = 3.31$ compared to the clean airfoil. The case with additional plain flap increases both maximum angle of attack ($\Delta\alpha_{max} = 0.75°$) and maximum lift coefficient

($\Delta c_{L,max} = 0.11$). Furthermore, the lift coefficient is increased by $\Delta c_L = 0.28$ in the linear range. If the design parameters of the fixed-vane flap would not be fixed to the results from the outboard optimization but free for optimization, the maximum lift coefficient could be further increased as the dashed lines indicate.

6.2 Wing-body

Based on the sectional optimization results, the high-lift system is integrated into the geometric model of the aircraft. In the initial 3D simulations, a wing-body model is assessed. Therefore, the gap between the inboard and the outboard Krueger flap is sealed with a fillet (figure 11). Towards the inboard side, the Krueger flap is cut off resulting in a gap between the belly fairing and the Krueger flap. The surface mesh of the main wing and the high-lift devices (except the side panels) is fully structured, whereas the fuselage is meshed with triangles. The hybrid mesh approach results in a mesh size of about 44 million points.
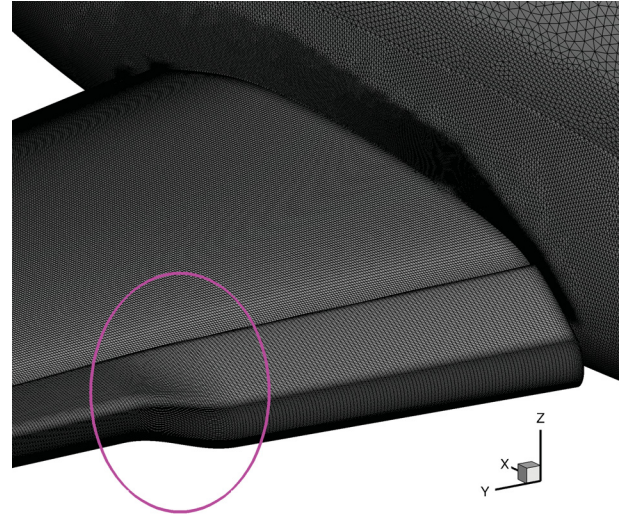

Figure 11: Geometry and surface mesh of the inboard region with Krueger fillet

Figure 12(a) shows the surface pressure distribution and skin friction lines on the upper side of the baseline configuration at $\alpha = 6°$. Generally, the skin friction lines are aligned normal to the leading edges of the elements. A significant transportation of boundary layer towards the inboard at the main wing's rear, as known from the cruise wing, cannot be identified. On the vane and the flap leading edge, the skin friction lines are strongly directed towards the wing tip due to their high leading edge sweep. As

seen in the analysis of the sectional data, the flow is partially separated from the flap. At the outboard wing, the flow is strongly bent towards the inboard due to the low pressure above the vane and the flap. At the fuselage-wing junction, the skin friction lines are distracted away from the belly fairing. Flowfield visualizations indicate flow reversal above the front part of the main element. Raising the angle of attack to $\alpha = 10°$, the unfavorable fuselage-wing junction flow leads to severe flow separation on the main element (figure 12(b)), which significantly limits the maximum lift coefficient.
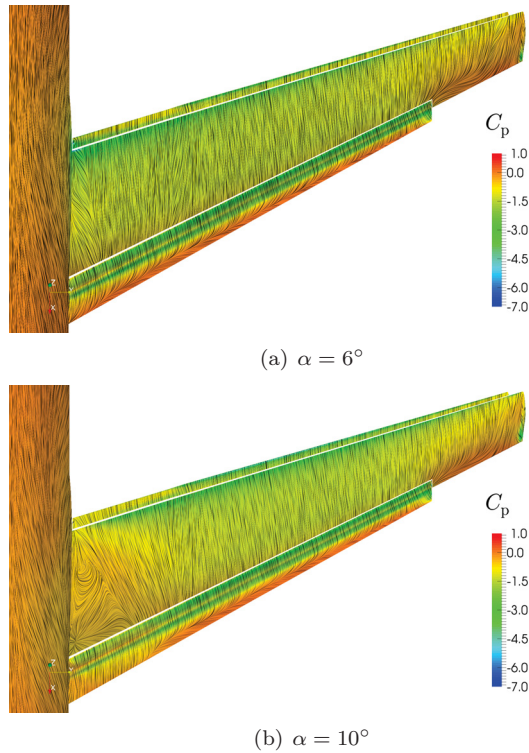

(a) $\alpha = 6°$

(b) $\alpha = 10°$

Figure 12: Surface pressure distribution and skin friction visualization on the wing-body baseline model

6.2.1 Wing-body junction flow

Figure 12(b) demonstrated that the initial landing configuration suffers from premature stall in the inboard region. In order to improve the maximum lift coefficient, several geometric modifications at the fuselage-wing junction were investigated. Even though the mechanism is not fully understood, several aspects lead to the unfavorable behavior in the inboard region. The negative sweep leads to a shift of the wing load towards the inboard. Furthermore, the rather thick boundary layer from the fuselage travels above the inner part of the main wing, as the fluid on the upper surface tends to flow towards the

wing tip. However, on the lower side, the flow tends towards the wing root. Consequently, the low momentum fluid, which recirculates below the Krueger flap is transported towards the inner Krueger flap tip, where it then passes over the main wing (figure 13(a)). Finally, the inner tip vortex of the Krueger flap is thought to have a negative effect on the flow conditions at the wing root. Since it is too weak to overcome the adverse pressure gradient above the main wing, the vortex bursts, which leads to high total pressure losses within the flow and eventually flow reversal. In order to re-engergize the flow at the wing root, a strake can be placed in front of the Krueger flap on the belly fairing. Figure 13(b) demonstrates how the region of total pressure loss is significantly reduced by the use of a strake. As a result, the maximum angle of attack and maximum lift coefficient are raised. An alternative way to improve the fuselage-wing junction flow is to close the gap between the Krueger flap and the belly fairing, as it is shown in figure 13(c)). Sealing the gap suppresses the Krueger flap's tip vortex and reduces the tendency of the recirculating flow below the Krueger flap to move towards the wing root. Consequently, the total pressure losses in the junction area are significantly reduced. Consequently, the separation is delayed. However, main wing stall still occurs due to trailing edge separation at the wing root of the main element. Figure 14 depicts the flow in the fuselage-wing junction at $\alpha = 17°$ in terms of streamlines colored with the Mach number. Furthermore, zones of total pressure losses are visualized by cutting planes. Both indicate that the flow separation originates from two sources. The first one occurs as early as $\alpha = 10°$ and can be traced back to the intersection of the main wing's leading edge with the belly fairing and the corner flow of the Krueger flap. Both corner flows are accompanied with high total pressure losses that weaken the boundary layer and eventually lead to trailing edge separation. However, the separation takes place about $\Delta\eta = 2\%$ outboard of the wing's trailing edge intersection with the belly fairing. This emphasizes the idea of the diverging channel effect at the wing root. However, as can be also seen from the streamlines, the opening gap in downstream direction between the wing root at the trailing edge and the streamlines coming from the wing root at the leading edge is being filled with low momentum boundary layer flow from the fuselage. The velocity of this boundary layer flow is further reduced due to the corner between the belly fairing and the wing and eventually leads to the second separation region, which is directly located at the wing root.
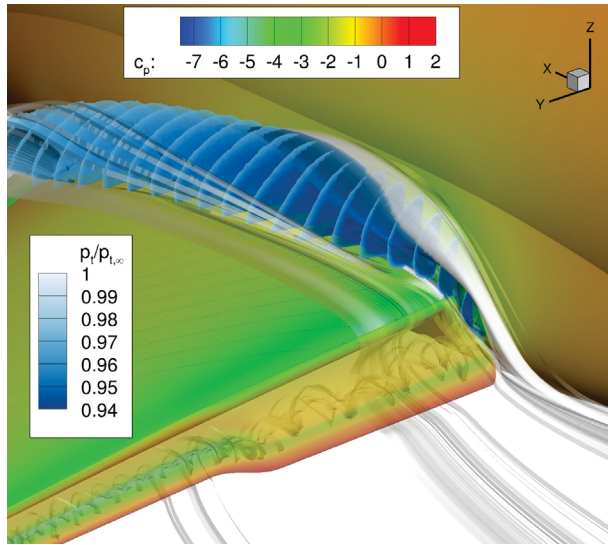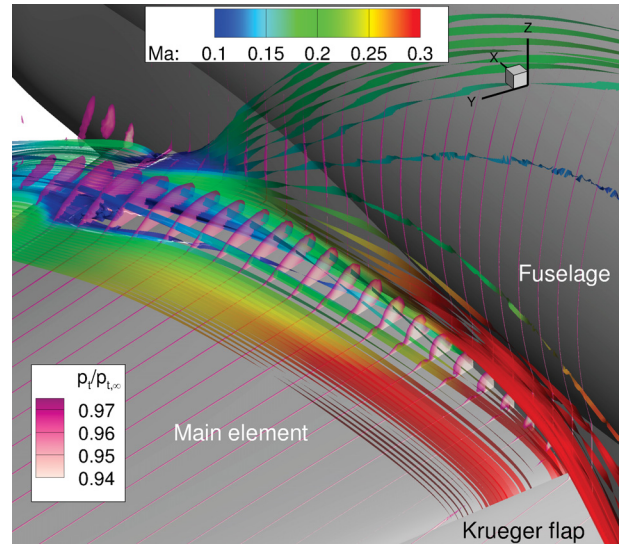
(a) Baseline
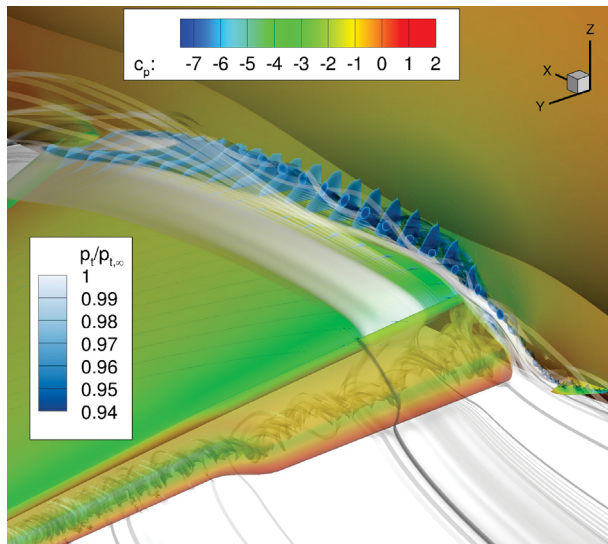
(b) Belly strake
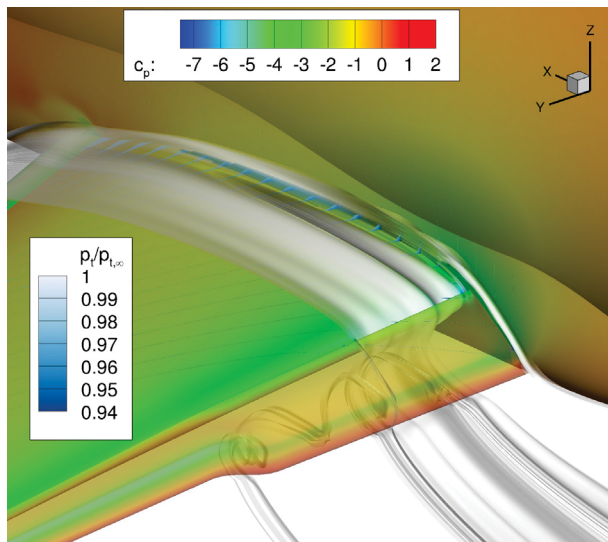
(c) Sealed gap between belly fairing and Krueger flap

Figure 13: Total pressure loss at fuselage-wing junction ($\alpha = 8°$)

Figure 14: Fuselage-wing junction flow at $\alpha = 17°$ for baseline configuration with sealed Krueger flap

6.2.2   2D vs. 3D comparison

Figure 15 compares the pressure distribution of the 3D wing-body simulations at $\alpha = 10°$ with the 2D computations at the design sections for the baseline configuration. Due to the induced angle of attack, the angle of attack of the 2D data, which are used for comparison are significantly lower than the one of the 3D simulation. In general, the data of both sections fit very well. Especially, the pressure distributions at $\eta = 0.56$ agree well. Both, 2D and 3D computations lead to a partial flap separation, which is represented almost identically by the pressure distributions on the flap. At $\eta = 0.22$, notable differences can be identified at the flap. Again, both computations lead to a trailing edge separation on the flap. However, the one in case of the 2D computation is significantly larger. Consequently, the pressure coefficient of the 2D computation is higher on the entire upper surface of the flap compared to the one from the 3D computation. It it not unusual that the 3D model of a swept wing behaves more robust against separation than the equivalent 2D geometry. Furthermore, it has to be noted that the inboard section is very close to the fuselage-wing junction, which might have an effect, too.
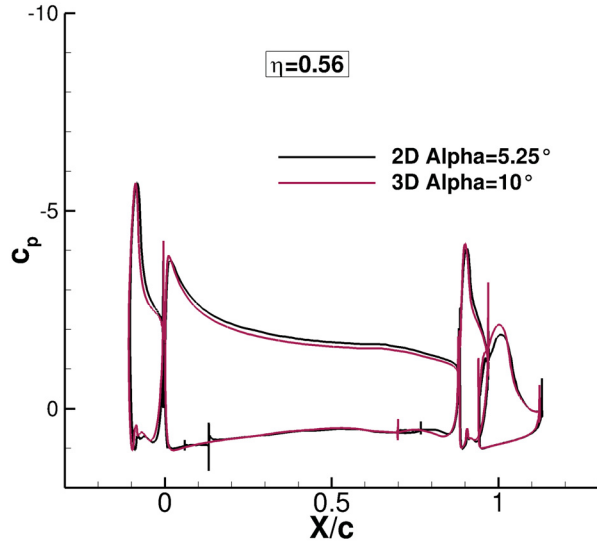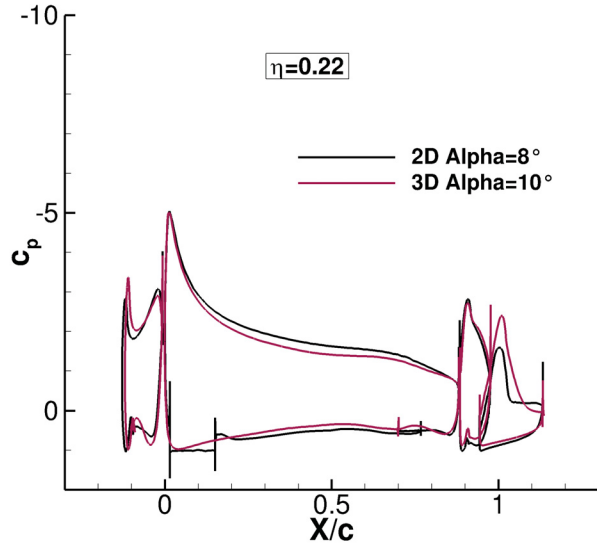
©2017

(a) $\eta = 0.56$

(b) $\eta = 0.22$

Figure 15: 3D vs. 2D comparison of pressure distributions at design sections

6.2.3 Baseline vs. plain flap

The 3D performance of the baseline case and the case with additional plain flap were compared on the wing-body model with sealed Krueger flap. Comparing their lift curves (figure 16) shows that the baseline case delivers a slightly better high-lift performance than the case with the plain flap. Both, the lift in the linear range as well as the maximum lift coefficient are higher ($C_{L,max,BSL} = 2.98$ vs. $C_{L,max,PF} = 2.94$), whereas the maximum angle of attack is identical. This behavior is somewhat unexpected as the additional degree of freedom due to the plain flap deflec-

tion is supposed to improve the high-lift performance. However, the fact that the case with plain flap is only superior in terms of maximum lift coefficient but inferior in terms of lift in the linear range regarding the optimization of the outboard section gives a possible explanation. Due to the induced angle of attack and the wing root stall, the maximum angle of attack of the outboard section, where the plain flap would become advantageous, is never reached in the 3D case. In order to benefit from the plain flap, one might have to change the optimization strategy, e.g. by changing the objective function. If the optimization aims at maximizing the lift coefficient at the angle of attack, which is the local effective angle of attack of the 3D configuration at stall, the optimization of the case with plain flap might lead to a better result.
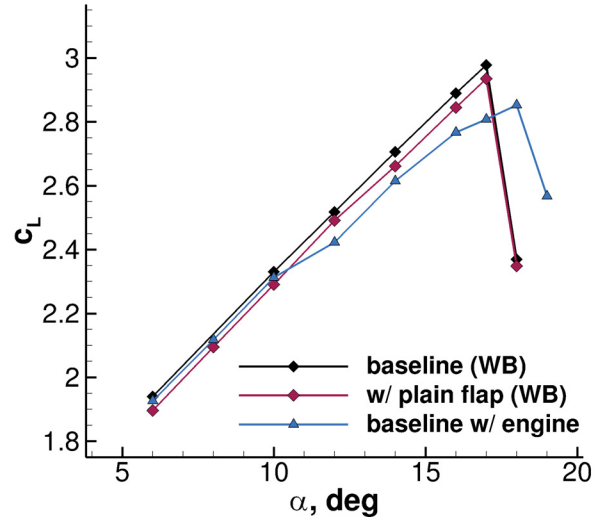

Figure 16: Lift curves of 3D models

6.3 Wing-body-nacelle

In order to estimate the high-lift performance of the landing configuration for the TuLam aircraft configuration, the baseline model was equipped with IAE V2500 engines. Therefore, the Krueger flaps were cut back as much as necessary in order to allow a deployment without collision. The positions of the nacelle strakes were taken from the engine's previous use on a different aircraft configuration and are not adapted.

Figure 16 compares the lift curve of the baseline configuration with engine to the one without engine. Up to an angle of $\alpha = 6°$, the lift loss due to the engine integration is low with $\Delta C_L \approx 0.01$. However, at $\alpha = 12°$, the lift reduction increases to $\Delta C_L \approx 0.10$. At this angle of attack, nacelle vortices emanate from the top of the nacelle. Especially the inner nacelle

vortex, which is located between the inner strake vortex and the outer Krueger tip vortex of the inboard Krueger flap (figure 17) is thought to have a negative effect on the lift generation as the suction peak of the vane and the flap are suddenly reduced further downstream (figure 18). Yet, the flow is not separated from the main element and actually reattaches locally to the flap at this position, as it is also shown by the skin friction lines in figure 17. Adapting the position of the inboard nacelle strakes might lead to an improvement of the flow in vicinity of the nacelle and thus reduce the lift losses. Even though the configuration with engine stalls one degree later than the one without engine, the maximum lift coefficient is reduced by 13 lift counts to $C_L = 2.85$. The stall mechanism is unchanged as the wing stalls due to flow separation at the wing root.
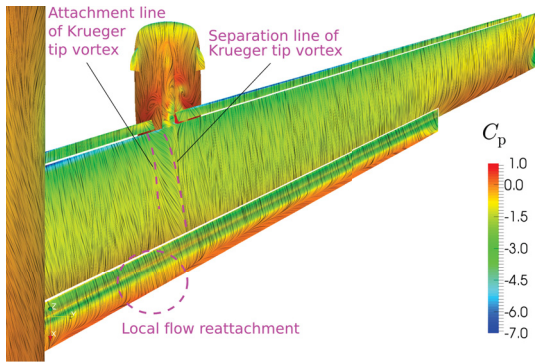

Figure 17: Surface pressure distribution and visualization of skin friction lines of baseline configuration with engine at $\alpha = 12°$
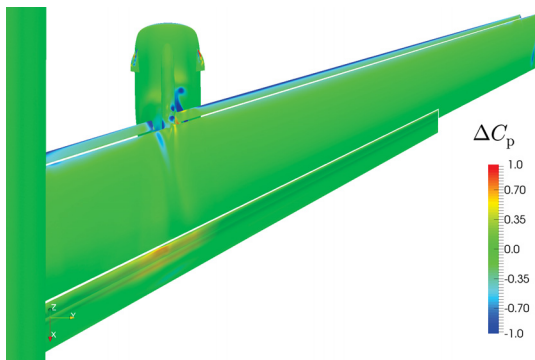

Figure 18: Difference in surface pressure distribution between $\alpha = 12°$ and $\alpha = 10°$ of baseline configuration with engine

7 Conclusions

A fully numerical aerodynamic high-lift design for a forward-swept natural laminar flow wing was successfully carried out. The chosen high-lift system, consisting of Krueger flaps and a fixed-vane flap were first optimized based on two wing sections while considering shielding requirements for the main wing's leading edge. The optimization results show significant constraints due to space limitations in the outboard section. The stall occurs due to flow separation at the Krueger flap, here. Since the inboard section, at which the shapes of the high-lift devices are less constrained, stalls due to a trailing edge separation on the main element, it is thought that the stall onset at the outboard section is related to the unfavorable deflection angle of the Krueger flap caused by the space limitations.

Subsequent to to the 2D optimizations, 3D RANS simulations of the wing-body model were performed. Sectional data from these simulations demonstrate good agreement with the 2D results. A slightly reduced severity of the flap separation in the inboard section suggests that additional potential of an $C_{L,max}$ increase exists if the 2D design is carried out more aggressively.

The high-lift performance gains due to the use of the additional plain flap, which were especially seen for the 2D inboard section, could not be observed in the 3D simulations. Changing the optimization objective as it was discussed in section 6.2.3 might lead to an advantageous performance of the wing-body model with plain flap.

The initial design of the fuselage-wing junction led to premature wing root stall, which could be significantly improved by sealing off the gap between the Krueger flap and the belly fairing. Since the flow separation at the wing root remains the reason for the wing stall, a shape optimization of the fuselage-wing junction could potentially lead to additional gains in the maximum lift coefficient.

Final simulations of the wing-body configuration with integrated engines delivered a satisfying maximum lift coefficient of $C_{L,max} = 2.85$. The stall mechanism remains unchanged compared to the wing-body model without engines, whereas the maximum lift coefficient is negatively affected by the engine integration. It is thought that further improvements of the maximum lift coefficient can be achieved by adapting the nacelle strake position.

References

[1] L. A. Walchli. High Lift and the Forward Swept Wing. Number 22, 1993.

[2] M. Bright, A. Korntheuer, S. Komadina, and J. Lin. Development of Advanced High Lift Leading Edge Technology for Laminar Flow Wings. Grapevine, Texas, USA, 2013. 51st AIAA Aerospace Sciences Meeting including the New Horizons Forum and Aerospace Exposition.

[3] P. K. C. Rudolph. High-Lift Systems on Commercial Subsonic Airliners. Contractor Report 4746, NASA, 1996.

[4] Boeing Commercial Airplane Group. High Reynolds Number Hybrid Laminar Flow Control (HLFC) Flight Experiment II. Aerodynamic Design. Contractor Report CR-1999-209324, NASA, 1999.

[5] J. Wild. Overview on the DeSiReH Project. Munich, Germany, 2013. 5th European Conference for Aeronautics and Space Sciences (EUCASS).

[6] P. Iannelli, J. Wild, M. Minervino, H. Strüber, F. Moens, and A. Vervliet. Design of a High-Lift System for a Laminar Wing . Munich, Germany, 2013. 5th European Conference for Aeronautics and Space Sciences (EUCASS).

[7] H. Strüber and J. Wild. Aerodynamic Design of a High-Lift System Compatible with a Natural Laminar Flow Wing within the DeSiReH Project . St. Petersburg, Russia, 2014. 29th Congress of the International Council of the Aeronautical Sciences.

[8] D. Franke and J. Wild. Aerodynamic Design of a Folded Krüger Device for a HLFC Wing. volume 132 of *Notes on Numerical Fluid Mechanics and Multidisciplinary Design*, pages 17–27. Springer Verlag, 2016.

[9] J. Raddatz and J. K. Fassbender. Block structured Navier-Stokes Solver FLOWer. In *MEGAFLOW - Numerical Flow Simulation for Aircraft Design*. Springer Verlag.

[10] T. Gerhold. Overview of the Hybrid RANS Code TAU. In N. Kroll and J. Fassbender, editors, *MEGAFLOW – Numerical Flow Simulation for Aircraft Design*, volume 89 of *Notes on Numerical Fluid Mechanics and Multidisciplinary Design*, pages 81–92. Springer, 2005.

[11] P.R. Spalart and S.R. Allmaras. A One–Equation Turbulence Model for Aerodynamic–Flows. AIAA Paper 92–439, 1992.

[12] P.R. Spalart and M. Shur. On the sensitization of turbulence models to rotation and curvature. volume 1 of *Aerospace Science and Technology*, pages 297–302. 1997.

[13] T. Rowan. Functional stability Analysis of Numerical Algorithms. Ph.d. thesis, Department of Computer Sciences, University of Texas at Austin, Austin, Texas, USA, 1990.

[14] J. Wild. Numerische Optimierung von zweidimensionalen Hochauftriebskonfigurationen durch Lösung der Navier-Stokes-Gleichungen. Forschungsbericht 2001-11, Institute of Aerodynamics and Flow Technology, German Aerospace Center, Braunschweig, Germany, 2001.

[15] W. Heinze, C. M. Österheld, and P. Horst. Multidisziplinäres Flugzeugentwurfsverfahren PrADO - Programmentwurf und Anwendung im Rahmen von Flugzeug-Konzeptstudien. In Deutsche Gesellschaft für Luft-und Raumfahrt (DGLR), editor, *DGLR-Jahrbuch 2001*, volume 3, pages 1701–1712. Bonn, 2001.

[16] J. Wild, J. Brezillon, O. Amoignon, J. Quest, F. Moens, and D. Quagliarella. Advanced Design by Numerical Methods and Wind Tunnel Verification within the European High-Lift Program. *Journal of Aircraft*, 46:157–167, 2009.

[17] D. Keller and J. Wild. High-lift concepts compatible with laminar flow wings. DLR-Interner Bericht DLR-IB 124-2014.

[18] T.L.B. Tamigniaux, S.E. Stark, and G.W. Brune. An experimental investigation of the insect shielding effectiveness of a Krueger flap/wing airfoil configuration. Monterey, CA., USA, 1987. 5th Applied Aerodynamics Conference.

[19] A.M.O. Smith. High-Lift Aerodynamics. *Journal of Aircraft*, 12(6):501–530, 1975.